

# Physics-informed Neural Networks with Periodic Activation Functions for Solute Transport in Heterogeneous Porous Media

Salah A Faroughi<sup>a,\*</sup>, Pingki Datta<sup>a</sup>, Seyed Kourosh Mahjour<sup>a</sup>, Shirko Faroughi<sup>b</sup>

<sup>a</sup>*Geo-Intelligence Laboratory, Ingram School of Engineering, Texas State University, San Marcos, Texas, 78666, USA*

<sup>b</sup>*Department of Mechanical Engineering, School of Engineering, Urmia University of Technology, Urmia, Iran*

---

## Abstract

Solute transport in porous media is relevant to a wide range of applications in hydrogeology, geothermal energy, underground CO<sub>2</sub> storage, and a variety of chemical engineering systems. Due to the complexity of solute transport in heterogeneous porous media, traditional solvers require high resolution meshing and are therefore expensive computationally. This study explores the application of a mesh-free method based on deep learning to accelerate the simulation of solute transport. We employ Physics-informed Neural Networks (PiNN) to solve solute transport problems in homogeneous and heterogeneous porous media governed by the advection-dispersion equation. Unlike traditional neural networks that learn from large training datasets, PiNNs only leverage the strong form mathematical models to simultaneously solve for multiple dependent or independent field variables (e.g., pressure and solute concentration fields). In this study, we construct PiNN using a periodic activation function to better represent the complex physical signals (i.e., pressure) and their derivatives (i.e., velocity). Several case studies are designed with the intention of investigating the proposed PiNN's capability to handle different degrees of complexity. A manual hyperparameter tuning method is used to find the best PiNN architecture for each test case. Point-wise error and mean square error (MSE) measures are employed to assess the performance of PiNNs' predictions against the ground truth solutions obtained analytically or numerically using the finite element method. Our findings show that the predictions of PiNN are in good agreement with the ground truth solutions while reducing computational complexity and cost by, at least, three orders of magnitude.

**Keywords:** Physics-informed Neural Networks, Solute Transport, Heterogeneous Porous Media, Advection-Dispersion Equation, Deep Learning, Scientific Computing

---

## 1. Introduction

Solute transport in porous media is crucial in many environmental and reservoir engineering applications, including risk and safety assessment of groundwater contamination [1], secondary recovery processes in petroleum reservoirs [2], geological storage of radioactive waste [3], hydrogen [4], and carbon dioxide [5], just to name a few [6]. It is a complicated process due to the varied temporal and spatial transport characteristics of the flow network [7]. These features can be divided into flowing areas influenced mostly by advection and stagnant regions governed mainly by dispersion [8]. The process is considerably more complicated in heterogeneous porous media, because all the available pore space does not contribute to flow uniformly; certain locations are dead ends, or transport is extremely sluggish due to an inadequate connection to the main flow channels [9]. Despite a conceptual understanding of the significance of multi-component solute transport mechanisms in porous media in general, attempts to conduct reliable experimental investigations are hindered by several barriers, resulting in a dearth of published information. The major causes are the technical difficulty of creating flow conditions and pore space connection under-regulated laboratory or in-situ test circumstances [10]. Hence, a system of field equations, which are numerically represented by partial differential equations (PDEs), is practically the only tool to predict the behavior of such non-linear flows in interconnected systems. In solute transport studies, traditional solvers, including finite element (FEM), finite difference (FDM), and finite volume methods (FVM), have been proposed to solve the governing PDEs. For example, Zhang et al. [11] suggested a 1D model based on FEM for multi-component solute transport in saturated soil. Bagalkot and Suresh Kumar [12] presented a 1D numerical evaluation of the FDM for multi-species radionuclide transport in a single horizontally coupled fracture-matrix system. Mostaghimi et al. [13] and Maheshwari et al. [14] investigated the effect of pore structure heterogeneity on reactive transport using a 3D pore scale model based on FVM. Although most large-scale calculations still use FEM, FDM, or FVM, they require high resolution meshing to describe the geometry of the domain being represented. Because the size of an elementary mesh is normally too large, discrete domain descriptions may also need the availability of efficient transport equations at the mesh scale and the consideration of unresolved subgrid-scale effects [15]. Hence, new methodologies

---

\*Corresponding author: salah.faroughi@txstate.edu

and algorithms, especially mesh-free methods based on deep learning, are required to accelerate the numerical simulations of solute transport through porous media.

Deep Learning (DL) methods have the potential to offer mesh-free solvers and address some of the aforementioned challenges. While most applications leverage DL (i.e., neural networks) to solve a lack of effective data modeling processes, explore vast design domains, and identify multidimensional connections [16, 17], there is a rising interest in using neural networks to solve PDEs [18, 19, 20, 21]. In general, there are three main neural network frameworks to accelerate scientific computing while considering underlying physics: Physics-guided Neural Networks (PgNN), Physics-informed Neural Networks (PiNN), and Physics-encoded Neural Networks (PeNN). Readers are referred to a recent review by Faroughi et al. [22], where different neural network frameworks are compared head-to-head, and their challenges and limitations are thoroughly discussed. In this study, we adopt PiNN due to its straightforward mechanism to integrate underlying physics in comparison to other approaches. By combining a loss function comprised of the residuals of physics equations, initial conditions and boundary restrictions, PiNN-based models adhere to physical laws. They employ automated differentiation to differentiate the outputs of neural networks with respect to their inputs (i.e., spatiotemporal coordinates and model parameters) [23]. The network can estimate the solution with high precision by minimizing the loss function [24]. Therefore, PiNN provides the foundation for a mesh-free solver that incorporates long-standing advances in mathematical physics into DL [18].

Raissi et al. [25] developed PiNN as a novel computing paradigm for both forward and inverse modeling in a series of studies [18, 25, 26]. Raissi et al. [26] developed a PiNN framework, dubbed hidden fluid mechanics (HFM), to encode the physical laws governing fluid flows, i.e., the Navier-Stokes equations. They leveraged underlying conservation laws to derive hidden quantities of objective functions such as velocity and pressure fields from spatiotemporal visualizations of a passive scalar concentration in arbitrarily complex domains. Their technique accurately predicted 2D and 3D pressure and velocity fields in benchmark problems inspired by real-world applications. Since then, PiNN and its different variants have been aggressively applied to different fields, including porous media flows. Almajid and Abu-Al-Saud [27] employed the PiNN framework to solve both the forward and inverse problems of the Buckley-Leverett PDE equation representing two-phase flow in porous media. In order to test their implementation, they applied the classic problem of gas drainage via a porous water-filled medium. Several cases were examined to demonstrate the significance of the connectivity between observable data and PiNNs for various parameter spaces. According to their results, PiNNs are capable of capturing the solution’s broad trend even without observed data, but their precision and accuracy improve significantly with observed data. Hanna et al. [28] employed PiNN to simulate 1D and 2D two-phase flow in porous media based on a new residual-based adaptive algorithm. Applying the PDE residual to build a probability density function from which additional collocation points are taken and added to the training set was fundamental to their work. The approach was individually applied to each PDE in the coupled system, considering the different collocation points for each PDE. In addition, the method was applied to enrich the points used to capture the initial and boundary conditions. They claimed that their approach yielded superior results with less generalization error than the conventional PiNN with fixed collocation points. Haghighat et al. [29] introduced a PiNN method to solve the coupled flow and deformation equations in porous media for single-phase and multiphase flow. Due to the problem’s dynamic nature, they reported a dimensionless form of the coupled governing equations for the optimizer. In addition, they presented a way for sequential training based on the stress-split algorithms of poromechanics. They demonstrated that sequential training based on stress-split performs well for a variety of problems, whereas the conventional strain-split algorithm exhibits instability comparable to that observed for FEM solvers. He et al. [30] extended a PiNN-based parameter estimation method to integrate multiphysics measurement. They studied a subsurface transport problem with sparse conductivity, a hydraulic head, and solute concentration. In their methodology, they employed the Darcy and advection-dispersion equations in conjunction with data to train deep neural networks, reflecting space-dependent conductivity, head, and concentration fields. They proved that the proposed PiNN method considerably increased the accuracy of parameter and state estimates for sparse data when compared to conventional deep neural networks trained with data alone. He and Tartakovsky [31] also suggested a discretization-free technique based on PiNN for solving the coupled advection-dispersion equations and Darcy flow equation with space-dependent hydraulic conductivity. They used PiNN for both one-dimensional and two-dimensional forward advection-dispersion equations and compared its performance for various Peclet numbers (Pe) with analytical and numerical solutions. They found that the PiNN was accurate with errors of less than 1% and outperformed other discretization-based approaches for large Pe. In addition, they proved that the PiNN remained accurate for backward advection-dispersion equations, with relative errors below 5% in the majority of instances. In another study, Vadyala et al. [32] implemented PiNN with the use of a machine learning framework such that it can be employed in reduced-order models to reduce epistemic (model-form) ambiguity associated with the advection equation. They demonstrated that PiNN provided an accurate and consistent approximation with the PDEs. Additionally, they showed that PiNN could transform the physics simulation field by enabling real-time physics simulation and geometry optimization without costly and time-consuming simulations on large supercomputers.

Although there has been an increase in the application of PiNN to fluid flow studies in porous media, the application of PiNN to the advection-dispersion equation in heterogeneous porous media has received less

attention. The main objective of this study is to develop a PiNN model capable of predicting the pressure and solute concentration fields simultaneously in heterogeneous porous media. To this end, we construct PiNN using periodic activation functions to better represent the complex physical signals and their derivatives. Using this modification, the derivative of the network inherits the network's properties entirely, which enables supervising any derivative of the network with complex physical signals, such as solute transport in heterogeneous media. Several 1D and 2D test cases are examined to evaluate how well the proposed PiNN model can predict the major transport fields.

This paper is structured as follows: In Section 2, the underlying physics for solute transport in a porous medium is presented. Section 3 discusses the PiNN's algorithm with periodic activation functions to predict solute transport. In Section 4, the PiNN is deployed to several one-dimensional (1D) and two-dimensional (2D) case studies, and its predictions are examined by comparing with analytical and/or FEM solutions. Finally, in Section 5, we summarize the main conclusions of this work.

## 2. Underlying Physics

Solute transport in porous media is governed by three major mechanisms: advection, diffusion, and dispersion [33, 34, 35]. The mathematical formulation of the advection-diffusion-dispersion equation is explained briefly here in terms of implementing the flow and transport factors that affect the transport process. The mass conservation equation serves as the basis for the solute transport equation [36, 37] that reads as,

$$\nabla \cdot \mathbf{J} = -\frac{\partial}{\partial t}(\phi C), \quad (1)$$

where  $\mathbf{J}$  is the solute mass flux,  $\phi$  is the porosity, and  $C$  is the solute concentration. The flux  $\mathbf{J}$  contains two mechanisms,

$$\mathbf{J} = -\phi D \nabla C + \mathbf{u}(\phi C), \quad (2)$$

where the first term refers to the diffusion flux, and the second term refers to the advection flux [38, 39]. In Eq. (2),  $D$  is the molecular diffusion coefficient ( $D = D_0$ ), and  $\mathbf{u} = [u_x, u_y, u_z]$  is the velocity vector of pore fluid flow computed using Darcy's law,

$$\mathbf{u} = \mathbf{q}/\phi = -\frac{k(x, y, z)}{\mu\phi} \nabla P, \quad (3)$$

where  $\mathbf{q}$  is the Darcy's flux,  $P$  refers to the pressure field,  $k(x, y, z)$  is the permeability, and  $\mu$  is the fluid viscosity. To include the impact of dispersion, the diffusion coefficient in Eq. 2 can be changed to

$$D = D_0 + \alpha U, \quad (4)$$

where  $\alpha$  is known as the dynamic dispersivity,  $D$  is now called the hydrodynamic dispersion coefficient, and  $U$  is the magnitude of fluid velocity defined as  $U = \sqrt{u_x^2 + u_y^2 + u_z^2}$ . We allow  $U$  to vary spatially for a heterogeneous porous medium where  $\mathbf{u}$  varies due to permeability changes [40, 41]. Substituting Eq. (2) into Eq. (1) leads to

$$\nabla \cdot [\phi D \nabla C] - \nabla \cdot [\mathbf{u}(\phi C)] = \frac{\partial(\phi C)}{\partial t}, \quad (5)$$

which can be rewritten as,

$$\nabla \cdot [\phi D \nabla C] - (\nabla \cdot \mathbf{u})(\phi C) - \mathbf{u} \cdot \nabla(\phi C) = \frac{\partial(\phi C)}{\partial t}, \quad (6)$$

that incorporates diffusion, dispersion, and advection transports and serves as the foundation of solute transport in porous media [42]. If the solute transport process has no effect on fluid density (i.e., incompressible flow,  $\nabla \cdot \mathbf{u} = 0$ ), the velocity field can be calculated independently of the solute concentration using Darcy's law, and Eq. (6) reduces to,

$$\nabla \cdot [\phi D \nabla C] - \mathbf{u} \cdot \nabla(\phi C) = \frac{\partial(\phi C)}{\partial t}. \quad (7)$$

The flow incompressibility condition generates an equation for computing the pressure field as,

$$\nabla \cdot \mathbf{u} = \nabla \cdot \left( -\frac{k(x, y, z)}{\mu\phi} \nabla P \right) = 0, \quad (8)$$

that reads as,

$$\frac{\partial}{\partial x} \left[ \zeta(x, y, z) \frac{\partial P}{\partial x} \right] + \frac{\partial}{\partial y} \left[ \zeta(x, y, z) \frac{\partial P}{\partial y} \right] + \frac{\partial}{\partial z} \left[ \zeta(x, y, z) \frac{\partial P}{\partial z} \right] = 0, \quad (9)$$

for three-dimensional (3D) flow problems, where

$$\zeta(x, y, z) = \frac{k(x, y, z)}{\mu\phi}. \quad (10)$$

Equations (7) and (9) together form the governing equations for the concentration and pressure fields in a porous medium with a heterogeneous permeability distribution [42].

### 3. Methodology

In this study, we leverage Physics-informed Neural Networks (PiNN) [18, 17] to resolve the solute transport in porous media, which is governed by a strong mathematical form consisting of the pressure and advection-dispersion equations as well as the relevant initial and boundary conditions. Unlike Physics-guided Neural Networks (PgNNs), PiNN is a mesh-free solution learning method that does not need labeled datasets [22]. In PiNNs, the underlying physics is included outside of the neural network architecture to constrain the model during training and ensure that the outputs follow given physical laws. The most common method to emulate this process is through a weakly imposed penalty loss that penalizes the network when it does not follow the physical constraints [25, 43, 44].

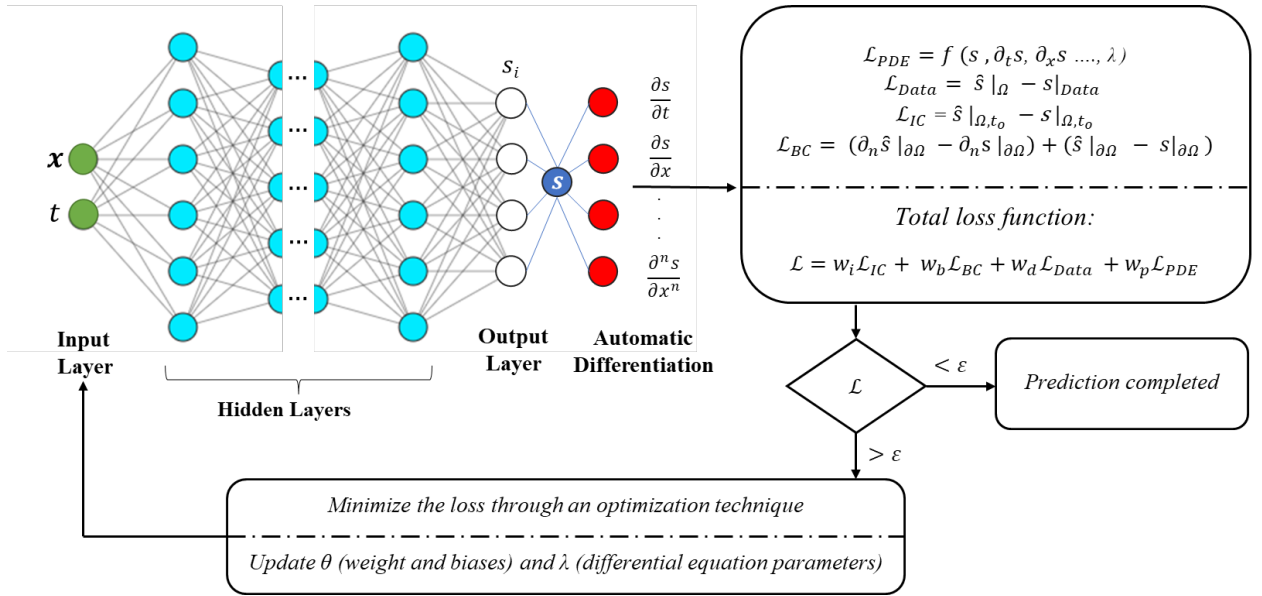


Figure 1: A schematic architecture of Physics-informed Neural Networks (PiNNs). The network digests spatiotemporal coordinates,  $(\mathbf{x}, t)$ , as inputs to predict a solution set,  $\mathbf{s}$ , as an approximate to the ground truth solution,  $\hat{\mathbf{s}}$ . The automatic differentiation (AD) is then used to generate the derivatives of the predicted solution  $\mathbf{s}$  with respect to inputs. These derivatives are used to formulate the residuals of the governing equations in the loss function weighted by different coefficients.  $\theta$  and  $\lambda$  are the learnable parameters for weights/biases and unknown PDE parameters, respectively, that can be learned simultaneously while minimizing the loss function.

A schematic representation of our PiNN architecture is illustrated in Fig. 1. As illustrated, a PiNN consists of three elements: a neural network (NN), an automatic differentiation (AD) layer, and a feedback mechanism informed by physics [45]. A neural network is first built in order to digest the spatiotemporal features (i.e.,  $\mathbf{x}$  and  $t$ ) as input parameters and approximate the solution,  $s(\mathbf{x}, t)$ , of a phenomenon described by PDEs with known boundary values. Assume that  $\mathbb{N}_L(\mathbf{x}) : \mathbb{R}^{d_{in}} \rightarrow \mathbb{R}^{d_{out}}$  be a  $L$ -layer neural network, or a  $(L - 1)$ -hidden layer neural network, with  $N_l$  neurons in the  $l^{th}$  layer ( $N_0 = d_{in}$ ,  $N_L = d_{out}$ ) [46]. Each layer in the NN is associated with its own weight matrix  $\mathbf{W}^l \in \mathbb{R}^{N_l \times N_{l-1}}$  and bias vector  $\mathbf{b}^l \in \mathbb{R}^{N_l}$ . The NN is recursively defined using an element-wise nonlinear activation function,  $\sigma$ , as follows, [47],

$$\text{Input layer: } \mathbb{N}_0(\mathbf{x}) = \mathbf{x} \in \mathbb{R}^{d_{in}}, \quad (11)$$

$$\text{Hidden layers: } \mathbb{N}_l(\mathbf{x}) = \sigma(\mathbf{W}^l \mathbb{N}_{l-1}(\mathbf{x}) + \mathbf{b}^l) \in \mathbb{R}^{N_l}, \text{ for } 1 \leq l \leq L - 1, \quad (12)$$

$$\text{Output layer: } \mathbb{N}_L(\mathbf{x}) = \mathbf{W}^L \mathbb{N}_{L-1}(\mathbf{x}) + \mathbf{b}^L \in \mathbb{R}^{d_{out}}, \quad (13)$$

where  $\sigma$  is commonly specified as the logistic sigmoid  $\sigma(x) = 1/(1 + \exp(-x))$ , hyperbolic tangent  $\sigma(x) = \tanh(x)$ , or the rectified linear unit,  $\sigma(x) = \max(x, 0)$  [46]. In this work, we propose to leverage periodic activation functions (e.g., sinusoidal),

$$\sigma(\mathbf{W}^l \mathbb{N}_{l-1}(\mathbf{x}) + \mathbf{b}^l) = \sin(\mathbf{W}^l \mathbb{N}_{l-1}(\mathbf{x}) + \mathbf{b}^l), \quad (14)$$



that are ideally suited for representing complex physical signals and their derivatives [48]. Using periodic activation functions, the derivative of a network behaves like the network itself (i.e., the derivative of the sine is a cosine that is a phase-shifted sine). As a result, the derivatives of the  $\mathbb{N}_L(\mathbf{x}) : \mathbb{R}^{d_{in}} \rightarrow \mathbb{R}^{d_{out}}$  inherit its properties that enable supervising any derivative of the network with complex physical signals, including boundary value problems [48]. In addition, it has been shown that NN with periodic activation functions converges significantly faster than baseline architectures [48].

The outputs of the NN are then fed into the automated differentiation (AD) layer, which is the central property of PiNNs. AD is employed to assess the derivatives of the network outputs with respect to the network inputs [49, 46, 23, 50]. Consider a strong mathematical form with a PDE specified on the domain  $\Omega$  and parametrized by  $\lambda$ ,

$$f(\mathbf{x}, t : \Delta s; \lambda) = 0, \quad \mathbf{x} \in \Omega, \quad (15)$$

and boundary conditions (e.g., Dirichlet, Neumann, Robin boundary condition, etc.) specified on the boundary of the domain  $\partial\Omega$ ,

$$\psi(\mathbf{s}(\mathbf{x}, t)) = 0, \quad \mathbf{x} \in \partial\Omega, \quad (16)$$

where  $\mathbf{s}$  is the unknown solution, and  $\Delta$  represents the linear or nonlinear differential operator (e.g.,  $\frac{\partial}{\partial t}$ ,  $\frac{\partial}{\partial x}$ ,  $\frac{\partial^2}{\partial x^2}$ , etc.). The initial condition can be considered as a kind of Dirichlet boundary condition on the spatiotemporal domain. AD is used to apply  $\Delta$  and  $\psi$  operators on the neural network with respect to inputs, i.e.,  $\mathbf{x}$  and  $t$ , and generate the required terms in the loss function in order to optimize the PDE solution,  $\mathbf{s}$ . Lastly, a feedback mechanism is constructed to minimize the loss terms through optimizations. The total loss term is defined as [51, 50],

$$\mathcal{L} = w_i \mathcal{L}_{IC} + w_b \mathcal{L}_{BC} + w_d \mathcal{L}_{Data} + w_p \mathcal{L}_{PDE}, \quad (17)$$

where  $w_i$ ,  $w_b$ ,  $w_d$ , and  $w_p$ , are referred to as the weights for the loss due to the initial conditions, boundary conditions, labeled data, if any, and PDEs, respectively. The individual loss terms are computed as,

$$\mathcal{L}_{IC} = \frac{1}{N_i} \sum_{i=1}^{N_i} (\hat{s}|_{\Omega, t_0} - s|_{\Omega, t_0})^2, \quad (18)$$

$$\mathcal{L}_{BC} = \frac{1}{N_b} \sum_{i=1}^{N_b} ((\partial_n \hat{s}|_{\partial\Omega} - \partial_n s|_{\partial\Omega}) - (\hat{s}|_{\partial\Omega} - s|_{\partial\Omega}))^2, \quad (19)$$

$$\mathcal{L}_{Data} = \frac{1}{N_d} \sum_{i=1}^{N_d} (\hat{s}|_{\Omega} - s|_{Data})^2, \quad (20)$$

$$\mathcal{L}_{PDE} = \frac{1}{N_p} \sum_{i=1}^{N_p} (f(s, \partial_t s, \partial_x s, \dots, \lambda))^2, \quad (21)$$

where  $t_0$  is the initial time,  $s$  is the neural network prediction,  $\hat{s}$  is the ground truth solution,  $N_i$ ,  $N_b$ ,  $N_d$ , and  $N_p$  are, respectively, the number of spatiotemporal points representing the initial conditions, boundary conditions, labeled data, and collocation points (i.e., spatiotemporal points within the domain where the neural network prediction,  $s(\mathbf{x}, t)$  is checked against the constraints of PDEs). Finally, a gradient-based optimizer (e.g., the Limited-memory Broyden–Fletcher–Goldfarb–Shanno algorithm, L-BFGS) is employed to minimize the loss function. L-BFGS is a second-order optimizer that incorporates the Hessian matrix [52]. It is observed that L-BFGS can find a satisfactory solution for smooth PDE solutions faster than Adam and with fewer iterations [53, 54, 55]. At each iteration, the loss is checked against  $\mathcal{L} < \epsilon$ , where  $\epsilon$  is a specified tolerance. If the condition is not met, error backpropagation is implemented to update the learnable parameters ( $\theta$  and/or  $\lambda$ ). The entire cycle is repeated for a given number of iterations until the PiNN model produces learnable parameters with a loss error less than  $\epsilon$  [56]. PiNN training is more difficult than PgNN training, because PiNNs are composed of sophisticated non-convex and multi-objective loss functions, which may cause instability during optimization [57, 58].

We deployed the proposed PiNN to model solute transport in porous media predicting the pressure and concentration fields, i.e.,  $\mathbf{s} = (P, C)$ . We selected different PiNN architectures for the solute transport case studies in this paper because of the different PDEs and boundary conditions. However, we ensured that the selected PiNN had enough layers and width to estimate each target field. There are two critical normalization steps in the implementation of PiNNs that must be followed to ensure convergence to the correct solution [59]. The first is mapping the network's input and output variables to the interval  $[0, 1] \in \mathbb{R}$ . The second step is to scale the pressure and concentration PDEs such that all terms are in the same order (unity).

#### 4. Computational Experiments

In this section, we applied the proposed PiNN model to solve 1D and 2D solute transport phenomena under different conditions (i.e., a total of four computational experiments are explored). We validated the

PiNN's prediction against analytical and/or FEM solutions to examine the potential, capability, and accuracy of the PiNN model.

#### 4.1. Case 1: 1D solute transport with constant velocity

This test case explores solute transport in a 1D domain ( $x \in [0, L]$ ) representing an isotropic porous medium with a constant velocity field. As the steady-state velocity field is known, the governing equation, Eq. (7), reduced to,

$$\frac{\partial C}{\partial t} + u_x \frac{\partial C}{\partial x} = \frac{\partial}{\partial x} (D_x \frac{\partial C}{\partial x}), \quad 0 < x < L, \quad 0 < t < t_0, \quad (22)$$

where  $L = 1$  is the length of the domain,  $u_x = 0.5$  m/s is the steady state velocity field, and  $D_x = 0.02$  m<sup>2</sup>/s refers to the hydrodynamic dispersion coefficient in the  $x$  direction. For this case, we assume the following initial and boundary conditions,

$$\begin{cases} C(x, t) = 0; & t = 0, \\ C(x, t) = C_0; & x = 0, \\ \frac{\partial}{\partial x} C(x, t) = 0; & x = L. \end{cases} \quad (23)$$

where  $C_0 = 1.0$  kg/m is the injected concentration at  $x = 0$  (i.e., Dirichlet boundary condition). This 1D advection–dispersion can be solved analytically [60]. The analytical solution is,

$$C(x, t) = C_0 \left( 1 - 2 \exp\left(\frac{x u_x}{2 D_x} - \frac{u_x^2 t}{4 D_x}\right) \sum_{i=1}^{\infty} \frac{\beta_i \sin(\frac{\beta_i x}{L}) \exp(-\frac{\beta_i^2 D_x t}{L^2})}{\beta_i^2 + (\frac{u_x L}{2 D_x})^2 + \frac{u_x L}{2 D_x}} \right), \quad (24)$$

where  $\beta_i$  are the roots of,

$$\beta \cot \beta + \frac{u_x L}{2 D_x} = 0. \quad (25)$$

Equations (24) and (25) can be approximated using [36],

$$C(x, t) = C_0 A(x, t), \quad 0 < t \leq t_0, \quad (26)$$

where  $A(x, t)$  is computed as,

$$\begin{aligned} A(x, t) = & \frac{1}{2} \operatorname{erfc}\left(\frac{x - u_x t}{2 \sqrt{D_x t}}\right) + \frac{1}{2} \exp\left(\frac{u_x x}{D_x}\right) \operatorname{erfc}\left(\frac{x + u_x t}{2 \sqrt{D_x t}}\right) \\ & + \frac{1}{2} \left(2 + \frac{u_x (2L - x)}{D_x} + \frac{u_x^2 t}{D_x}\right) \exp\left(\frac{u_x L}{D_x}\right) \operatorname{erfc}\left(\frac{2L - x + u_x t}{2 \sqrt{D_x t}}\right) \\ & - \left(\frac{u_x^2 t}{\pi D_x}\right)^{\frac{1}{2}} \exp\left(\frac{u_x L}{D_x} - \frac{1}{4 D_x t} (2L - x + u_x t)^2\right). \end{aligned} \quad (27)$$

A PiNN with the periodic activation function and randomly distributed collocation points is then used to predict the solute transport in 1D described by Eq. (22) with the initial and boundary conditions given in Eq. (23). A manual hyperparameter tuning process was practiced to find the best architecture based on the MSE accuracy measures. This process yielded a network with four hidden layers with {32, 32, 16, 16} neurons per layer, and 5,000 spatiotemporal random points within  $0 \leq x \leq 1$  and  $0 \leq t \leq 10$  as the collocation points to enforce the PDE loss term. We used identical weights for all the loss terms ( $w_i = w_b = w_p = 1$ ), and used 5,000 spatiotemporal random points, collectively, to represent the boundary and initial conditions informing the loss terms.

Figure 2 represents the concentration field in the  $(\mathbf{x}, t)$  domain predicted by PiNN. The PiNN's prediction is also compared with the ground truth (analytical solution given by Eq. (27)) at different simulation times. The results of the comparison are shown in Fig. 2, which reveal a good agreement between PiNN's prediction and the ground truth resulting in  $MSE = 1.15 \times 10^{-6}$  for the considered spatiotemporal domain. This confirms the accuracy of the trained PiNN model for this simplified problem. In the next test cases, the PiNN is applied to more complex problems representing the complexity of solute transport in porous media.

#### 4.2. Case 2: 2D solute transport with constant velocity

This test case explores solute transport in a 2D rectangular domain ( $x \in [0, L]$ ,  $y \in [0, W]$ ) representing an isotropic porous medium with a constant velocity field,  $\mathbf{u} = (u_x, u_y)$ . Since the velocity field is given, the governing equation for solute transport, Eq. (7), is simplified to,

$$\frac{\partial C}{\partial t} + u_x \frac{\partial C}{\partial x} + u_y \frac{\partial C}{\partial y} = \frac{\partial}{\partial x} (D_x \frac{\partial C}{\partial x}) + \frac{\partial}{\partial y} (D_y \frac{\partial C}{\partial y}), \quad (28)$$

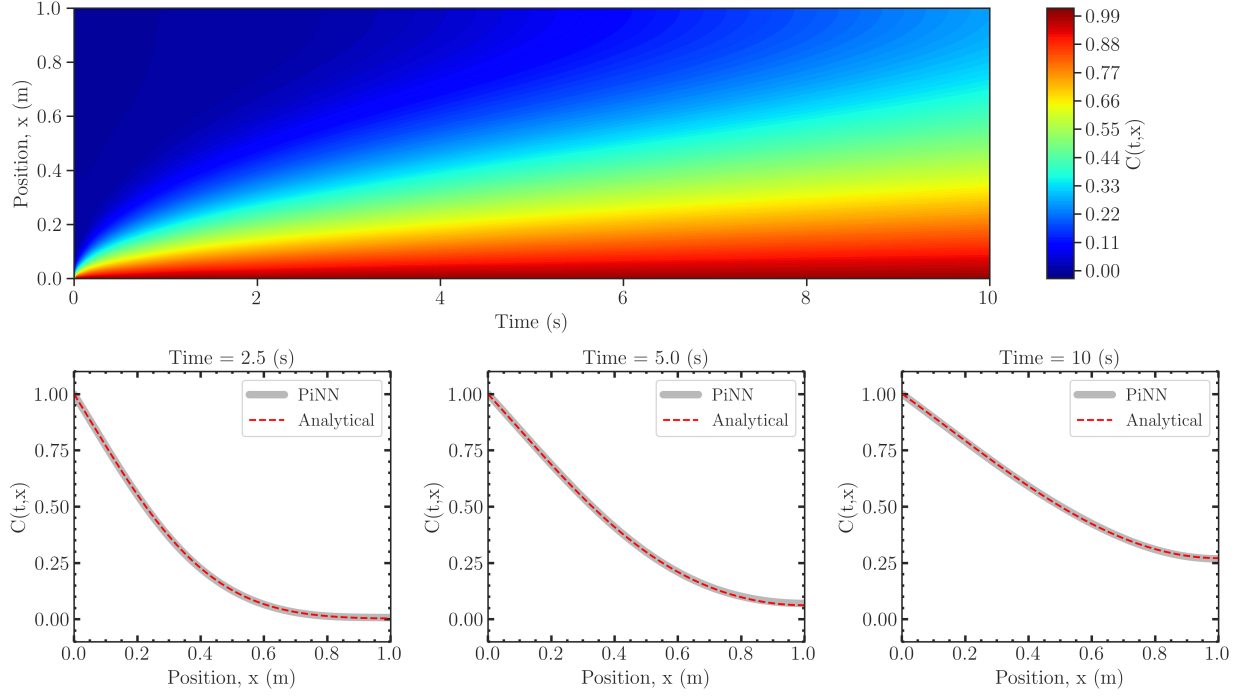


Figure 2: One-dimensional solute transport with a constant velocity field,  $u_x = 0.5 \text{ m/s}$ . The upper panel shows the concentration field predicted by PiNN within the spatiotemporal domain ( $0 \leq x \leq 1$ ,  $0 \leq t \leq 10$ ) at an injection rate of  $C_0 = 1 \text{ kg/m}$ . The lower panels show the comparison of PiNN's prediction with the ground truth obtained analytically using Eq. (26) at three different times. The comparison demonstrates a good agreement yielding  $MSE = 1.15 \times 10^{-6}$  for the entire spatiotemporal domain.

where  $D_y = D_x = 0.02 \text{ m}^2/\text{s}$  refers to the hydrodynamic dispersion coefficient in the  $y$  and  $x$  directions. As schematically shown in Fig. 3, the following initial and boundary conditions,

$$\begin{cases} C(x, y, t) = 0; & t = 0, \\ C(x, y, t) = C_0; & x = 0 \text{ and } y_1 \leq y \leq y_2, \\ C(x, y, t) = 0; & x = 0 \text{ and } y < y_1 \text{ and } y > y_2, \\ \frac{\partial}{\partial x} C(x, y, t) = 0; & x = L, \text{ and } 0 \leq y \leq W, \\ \frac{\partial}{\partial y} C(x, y, t) = 0; & y = 0 \text{ or } y = W, \text{ and } 0 \leq x \leq L, \end{cases} \quad (29)$$

are considered for this test case. The blue points on the left boundary bounded by  $y_1$  and  $y_2$  represent the positions of point-source solute injection at the rate of  $C_0 = 0.2 \text{ kg/m}^2$ . The other three sides of the domain are assigned as zero gradient boundaries, assuming a free outflow of solute. This 2D advection–dispersion problem defined by Eqs. (28) and (29) can be solved analytically [60],

$$C(x, y, t) = C_0 \sum_{n=0}^{\infty} L_n P_n \cos(\eta y) \left( \exp\left(\frac{x(u_x - \zeta)}{2D_x}\right) \text{erfc}\left(\frac{x - \zeta t}{2\sqrt{D_x t}}\right) + \exp\left(\frac{x(u_x + \zeta)}{2D_x}\right) \text{erfc}\left(\frac{x + \zeta t}{2\sqrt{D_x t}}\right) \right), \quad (30)$$

where  $L_n$  is defined as,

$$L_n = \begin{cases} \frac{1}{2}; & n = 0, \\ 1; & n > 0, \end{cases} \quad (31)$$

and  $P_n$  is computed as,

$$P_n = \begin{cases} (y_2 - y_1)/W; & n = 0, \\ (\sin(\eta y_2) - \sin(\eta y_1))/(n\pi); & n > 0, \end{cases} \quad (32)$$

where  $\eta$  and  $\zeta$ , respectively, are,

$$\eta = \frac{n\pi}{W} \quad (n = 0, 1, 2, 3, \dots), \quad \zeta = \sqrt{u_x^2 + 4\eta^2 D_x D_y}. \quad (33)$$

We first employed a PiNN with the periodic activation function and randomly distributed collocation points to predict the solute transport in the 2D domain ( $L = W = 1 \text{ m}$ ) considering dispersion only with  $D_x = D_y = 0.02 \text{ m}^2/\text{s}$  and  $\mathbf{u} = (u_x, u_y) = (0.0, 0.0) \text{ m/s}$  in Eq. (28) and the initial and boundary conditions given by Eq. (29). The solute injection rate is set to  $C_0 = 0.2 \text{ kg/m}^2$  between  $y_1 = 0.3 \text{ m}$  and  $y_2 = 0.7 \text{ m}$ . To determine the best PiNN architecture, a manual hyperparameter tuning approach was adopted. This approach

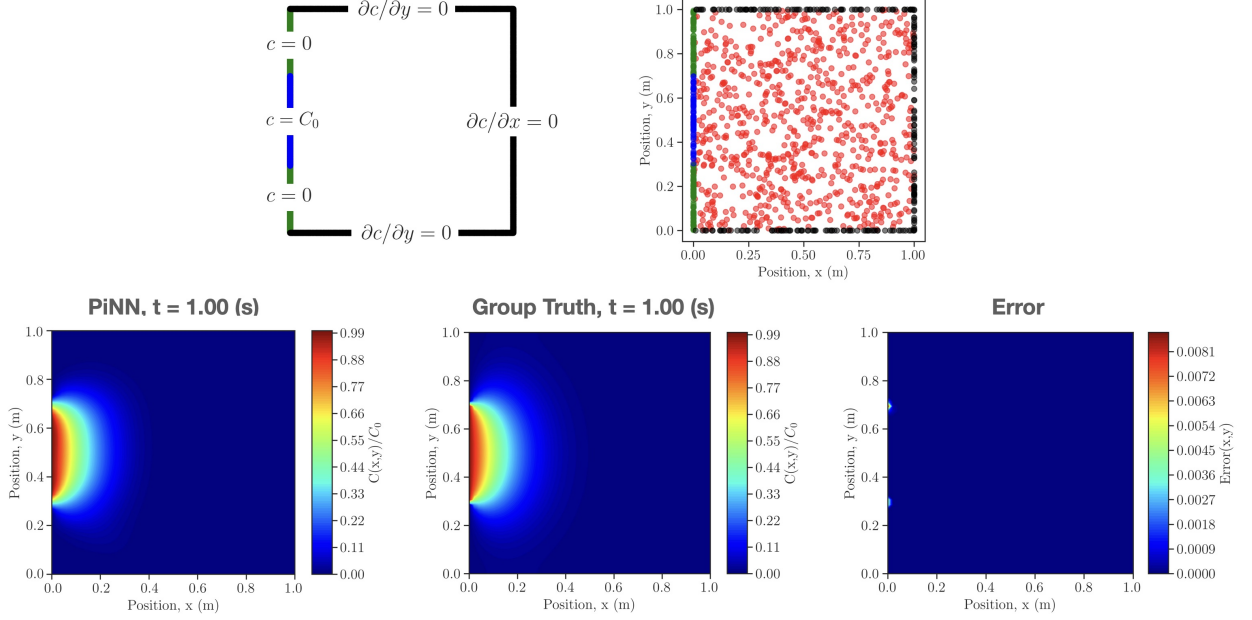


Figure 3: A comparison between PiNN's prediction and ground truth for solute transport in a 2D domain representing an isotropic porous medium considering  $D_x = D_y = 0.02 \text{ m}^2/\text{s}$ ,  $\mathbf{u} = (u_x, u_y) = (0.0, 0.0) \text{ m/s}$ , and solute injection rate of  $C_0 = 0.2 \text{ kg/m}^2$  between  $y_1 = 0.3 \text{ m}$  and  $y_2 = 0.7 \text{ m}$ . The upper panels show the domain with boundary conditions and distributions of randomly selected points on which different terms in the loss function are evaluated. The red dots represent the collocation points inside the domain corresponding to the loss term associated with the 2D solute transport PDE, and the blue, green, and black dots represent the points on the boundary of the domain corresponding to the loss terms associated with the boundary conditions. The lower panel shows the comparison between the PiNN's prediction of the concentration field at  $t = 1.00 \text{ s}$  and the ground truth obtained analytically using Eq. (30). The point-wise error shows the mismatch between the solutions yielding  $MSE = 0.67 \times 10^{-6}$ .

produced a network with four hidden layers and  $\{32, 16, 16, 16\}$  neurons per layer using 8,000 spatiotemporal random points within  $0 \leq x, y \leq 1$ ,  $0 \leq t \leq 1$  as collocation points to enforce the PDE loss term. We employed identical weights for the loss terms and utilized 8,000 spatiotemporal random points to represent the boundary and initial conditions informing the loss terms (sample selected points are shown in Fig. 3).

Figure 3 depicts the comparison of the 2D concentration field predicted by PiNN and the analytical solution given by Eq. (30). The point-wise error is also shown, which illustrates a good accordance between the analytic solution and PiNN's prediction yielding  $MSE = 0.67 \times 10^{-6}$ . It can be observed that the mismatch is close to zero everywhere in the domain except locations where extremely high concentration gradients exist (e.g., at points  $(0.0, 0.30)$  and  $(0.0, 0.70)$ ). This mismatch is due to a difficult-to-minimize optimization error, i.e., PiNN struggles to converge to ground truth solutions in high gradient areas [61].

A PiNN with the same architecture is then employed to model the advection–dispersion solute transport in 2D domains with  $D_x = D_y = 0.02 \text{ m}^2/\text{s}$  and  $\mathbf{u} = (u_x, u_y) = (0.5, 0.0) \text{ m/s}$ . The solute is injected again at a rate of  $C_0 = 0.2 \text{ kg/m}^2$  between  $y_1 = 0.3 \text{ m}$  and  $y_2 = 0.7 \text{ m}$ . The PiNN's predictions for the concentration field at different times ( $t = 0.25 \text{ s}$ ,  $0.50 \text{ s}$ ,  $0.75 \text{ s}$ ,  $1.00 \text{ s}$ ) are shown in Fig. 4. The concentration field at  $t = 1.00 \text{ s}$  is also compared with the analytical solution given by Eq. (28). The point-wise error shows that there is a good match between the PiNN's prediction and the analytical solution within the entire domain yielding  $MSE = 1.54 \times 10^{-6}$ .

The same PiNN model is also deployed to predict the solute transport in the 2D domain discussed above, but with line source injection (i.e.,  $y_1 = 0.0 \text{ m}$  and  $y_2 = 1.0 \text{ m}$ ). A comparison between the PiNN's prediction and analytical solution for the concentration field at  $t = 0.75 \text{ s}$  is shown in Fig. 5. As imposed by the boundary conditions, the contours are straight lines parallel to the  $x = 0$  boundary, which is predicted correctly by PiNN. The point-wise error shown in Fig. 5 demonstrates excellent agreement between the PiNN's prediction and the ground truth yielding  $MSE = 0.12 \times 10^{-6}$  that clearly signifies the PiNN model's capability to solve advection–dispersion equations.

#### 4.3. Case 3: 2D solute transport in homogeneous porous media

In this test case, the solute transport in a 2D homogeneous porous medium ( $x \in [0, L]$ ,  $y \in [0, W]$ ) is investigated. For this problem, assuming  $\zeta(x, y) = 1$ , the pressure equation defined by Eq. (9) reduces to,

$$\frac{\partial^2 P}{\partial x^2} + \frac{\partial^2 P}{\partial y^2} = 0, \quad (34)$$

that must be solved to determine the velocity field using Eq. (3). The governing equation for solute concentration remains the same as Eq. (28). The following boundary conditions are considered for the pressure field,

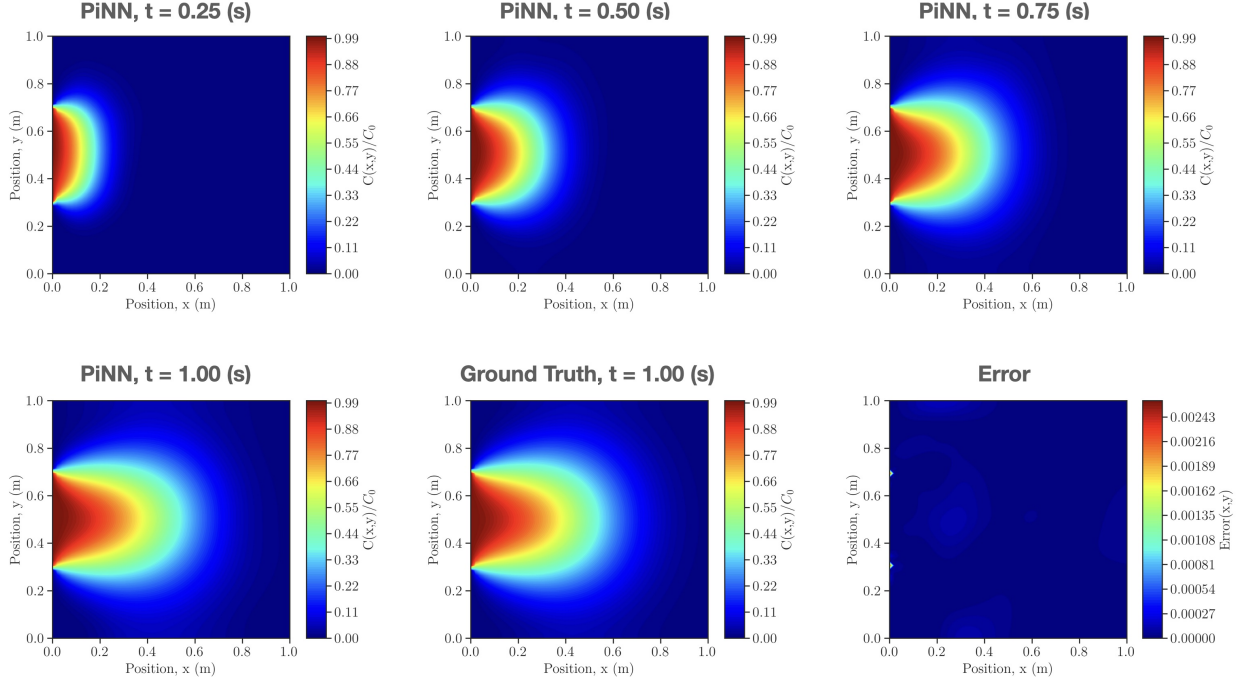


Figure 4: A comparison between PiNN's prediction and ground truth obtained analytically for the concentration field considering  $D_x = D_y = 0.02 \text{ m}^2/\text{s}$ ,  $\mathbf{u} = (u_x, u_y) = (0.5, 0.0) \text{ m/s}$ , and an injection rate of  $C_0 = 0.2 \text{ kg/m}^2$  between  $y_1 = 0.3 \text{ m}$  and  $y_2 = 0.7 \text{ m}$ . PiNN predictions are shown for  $t = 0.25 \text{ s}, 0.50 \text{ s}, 0.75 \text{ s}$ , and  $1.00 \text{ s}$ . At  $t = 1.00 \text{ s}$ , the PiNN's prediction is compared with the analytical solution obtained using Eq. (30). The point-wise error shows the mismatch between the solutions yielding  $MSE = 1.54 \times 10^{-6}$ .

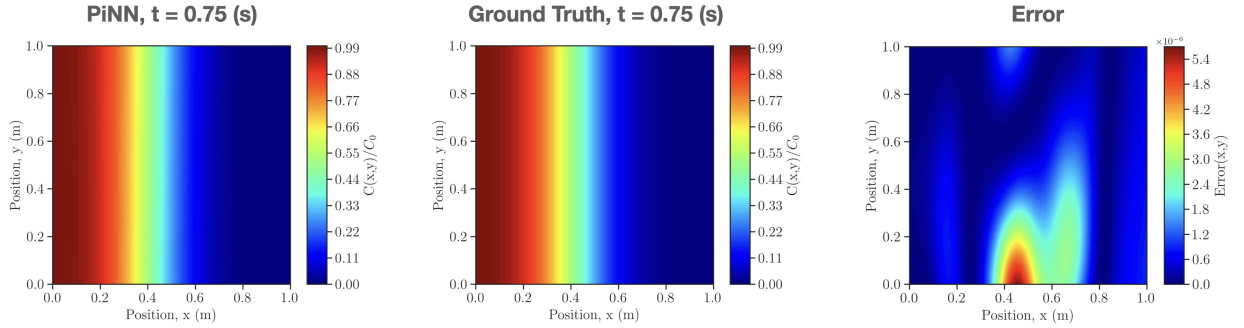


Figure 5: A comparison between PiNN's prediction and ground truth obtained analytically for the concentration field considering  $D_x = D_y = 0.02 \text{ m}^2/\text{s}$ ,  $\mathbf{u} = [u_x, u_y] = [0.5, 0.0] \text{ m/s}$ , and an injection rate of  $C_0 = 0.2 \text{ kg/m}^2$  between  $y_1 = 0.0 \text{ m}$  and  $y_2 = 1.0 \text{ m}$  (i.e., line-source injection). At  $t = 0.75 \text{ s}$ , the PiNN's prediction is validated against the analytical solution obtained using Eq. (30). The point-wise error shows the mismatch between the solutions yielding  $MSE = 0.12 \times 10^{-6}$ .

$$\begin{cases} P(x, y) = 1.0; & y = 0 \text{ or } y = W, \text{ and } 0 \leq x \leq L, \\ P(x, y) = 0.1; & x = 0 \text{ or } x = L, \text{ and } 0 \leq y \leq W, \end{cases} \quad (35)$$

and for the concentration field,

$$\begin{cases} C(x, y, t) = 0; & y = 0 \text{ or } y = W \text{ and } x < x_1 \text{ and } x > x_2, \\ C(x, y, t) = C_0; & y = 0 \text{ or } y = W \text{ and } x_1 \leq x \leq x_2, \\ \frac{\partial}{\partial x} C(x, y, t) = 0; & x = 0 \text{ or } x = L, \text{ and } 0 \leq y \leq W, \end{cases} \quad (36)$$

with  $C(x, y, t = 0) = 0$  as the initial condition. The pressure value at the corner points that belong to two perpendicular sides is set to 0.55, as additional constraints, to keep the symmetry. The ground truth solutions for pressure and concentration fields are obtained using FEM with a  $100 \times 100$  quadrilateral elements assuming  $L = W = 1 \text{ m}$ ,  $D_x = D_y = 0.02 \text{ m}^2/\text{s}$ , and  $C_0 = 0.2 \text{ kg/m}^2$ .

A PiNN with the periodic activation function and randomly distributed collocation points is employed to predict the solute transport in the 2D porous media described above. The PiNN's inputs are the spatiotemporal coordinates,  $(x, y, t)$ , and the outputs are the pressure and concentration fields, i.e.,  $\mathbf{s} = \{P, C\}$  in Fig. 1. The pressure and concentration fields are decoupled, therefore one may use two PiNNs side-by-side to solve this problem; however, training a PiNN with multiple outputs was more desirable in this study to minimize hyperparameter tuning. The hyperparameter tuning approach was again practiced manually to obtain the best PiNN architecture based on the MSE accuracy measures. This approach resulted in a network with five hidden layers and  $\{32, 16, 16, 8, 8\}$  neurons per layer using 12,000 spatiotemporal random points within  $0 \leq x, y \leq 1$ ,  $0 \leq t \leq 1$  as collocation points to enforce the pressure and concentration PDEs' loss terms. We employed identical weights for the loss terms and 12,000 spatiotemporal random points to represent the boundary and initial conditions informing the loss terms (sample selected points are shown in Fig. 6).

Figure 6 presents the ground truth (FEM solutions) and the PiNN's predictions for the pressure field, velocity field in the  $x$  direction, total velocity field, and flow streamlines for the homogeneous porous medium. The point-wise error is also shown for all the fields, which shows a good agreement between PiNN and FEM solutions. Figure 7 shows the same comparison, but for the concentration field at  $t = 1.00 \text{ s}$ . The point-wise error again shows a considerable agreement between the PiNN's prediction and the FEM solution yielding  $MSE = 0.24 \times 10^{-6}$ . These results imply that a PiNN can simultaneously solve for the pressure and solute concentration fields in a 2D homogeneous porous medium with a high accuracy. The following section explores the application of PiNN to solve the problem of solute transport in a heterogeneous porous medium.



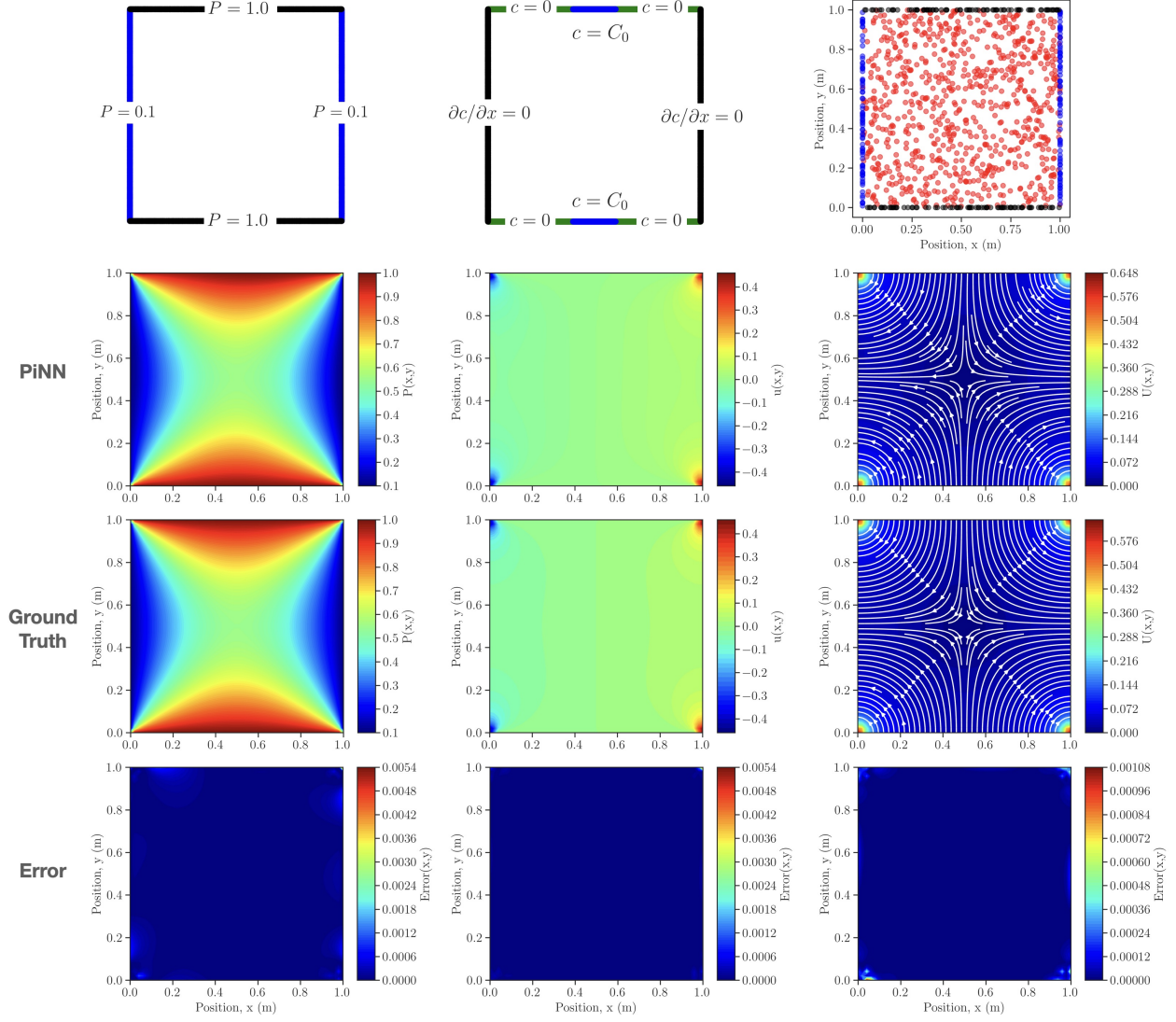


Figure 6: A comparison between PiNN's predictions and the ground truth for the pressure field in a 2D homogeneous porous medium. The upper panels show the domain with pressure and concentration boundary conditions as well as the distributions of randomly selected points on which different terms in the loss function are evaluated. The lower panels show the comparison between the PiNN's predictions and ground truth solutions obtained using FEM with  $100 \times 100$  quadrilateral elements for the pressure field, velocity field in the  $x$  direction, and total velocity field. The flow direction of the pore fluid is also represented by the streamlines. The point-wise error is also shown for each field to illustrate the mismatch between the solutions.

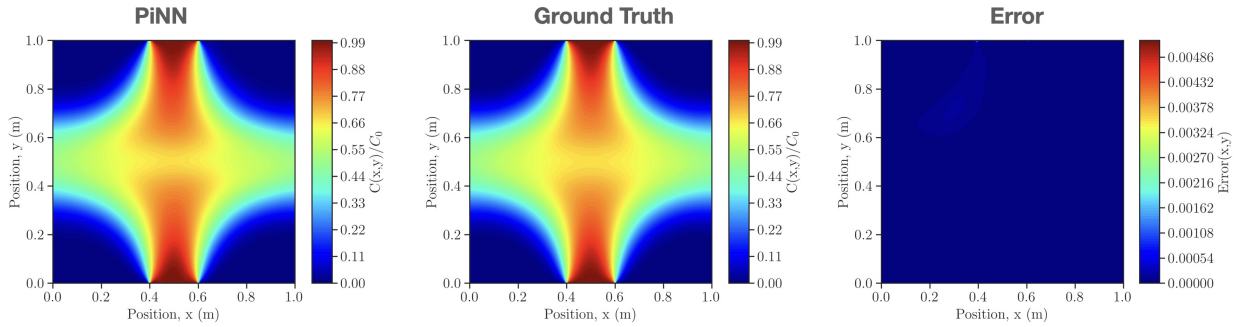


Figure 7: A comparison between the PiNN's prediction and ground truth for the concentration field at  $t = 1.00$  s in a 2D homogeneous porous medium considering  $D_x = D_y = 0.02 \text{ m}^2/\text{s}$  and  $C_0 = 0.2 \text{ kg/m}^3$ . The ground truth is obtained using FEM with  $100 \times 100$  quadrilateral elements. The point-wise error shows the mismatch between the solutions yielding  $MSE = 0.24 \times 10^{-6}$ .

#### 4.4. Case 4: 2D solute transport in heterogeneous porous media

In this test case, the solute transport is analyzed in a 2D rectangular domain ( $x \in [0, L]$ ,  $y \in [0, W]$ ) representing a heterogeneous porous medium, i.e., the permeability field  $k(x, y)$ , and hence,  $\zeta(x, y)$  in Eq. (9) vary spatially. The permeability field considered here is shown in Fig. 9. The initial and boundary conditions for this case are identical to those reported for Case 3. The pressure constraints at the corner points that

correspond to the two perpendicular sides are not maintained due to permeability. The ground truth solutions for pressure and concentration fields are determined using FEM with  $100 \times 100$  quadrilateral elements considering  $L = W = 1 \text{ m}$ ,  $\alpha = 0$ ,  $D_x = D_y = 0.02 \text{ m}^2/\text{s}$ ,  $\mu\phi = 0.001$ , and  $C_0 = 0.2 \text{ kg}/\text{m}^2$ .

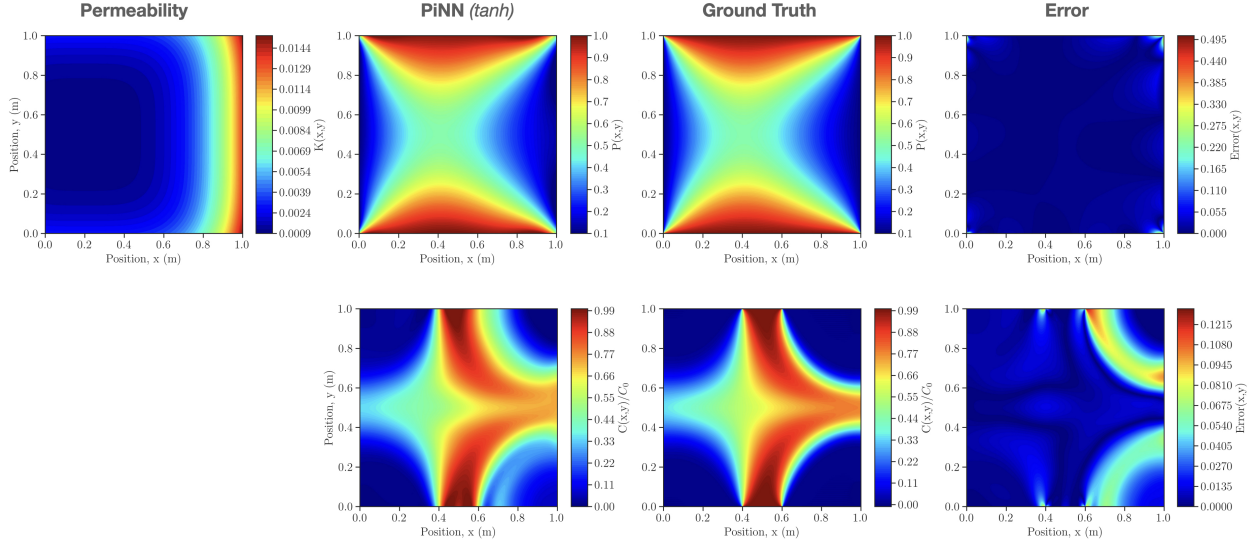


Figure 8: A comparison between the PiNN's predictions and ground truth solutions for solute transport in a heterogeneous porous medium with the given permeability field,  $k(x, y)$ . The comparison is illustrated for the pressure field as well as the concentration field at  $t = 1.00 \text{ s}$  considering  $D_x = D_y = 0.02 \text{ m}^2/\text{s}$ ,  $\alpha = 0$ ,  $\mu\phi = 0.001$ , and  $C_0 = 0.2 \text{ kg}/\text{m}^2$ . The PiNN model here uses the  $\tanh$  activation function, and the ground truth solutions are obtained using FEM with  $100 \times 100$  quadrilateral elements. The point-wise error for each field demonstrates that the PiNN has difficulty to converge to the ground truth solution when using the  $\tanh$  activation function. The disparity is more pronounced in the concentration field, which is caused by the rapid variation of the velocity field caused by heterogeneities.

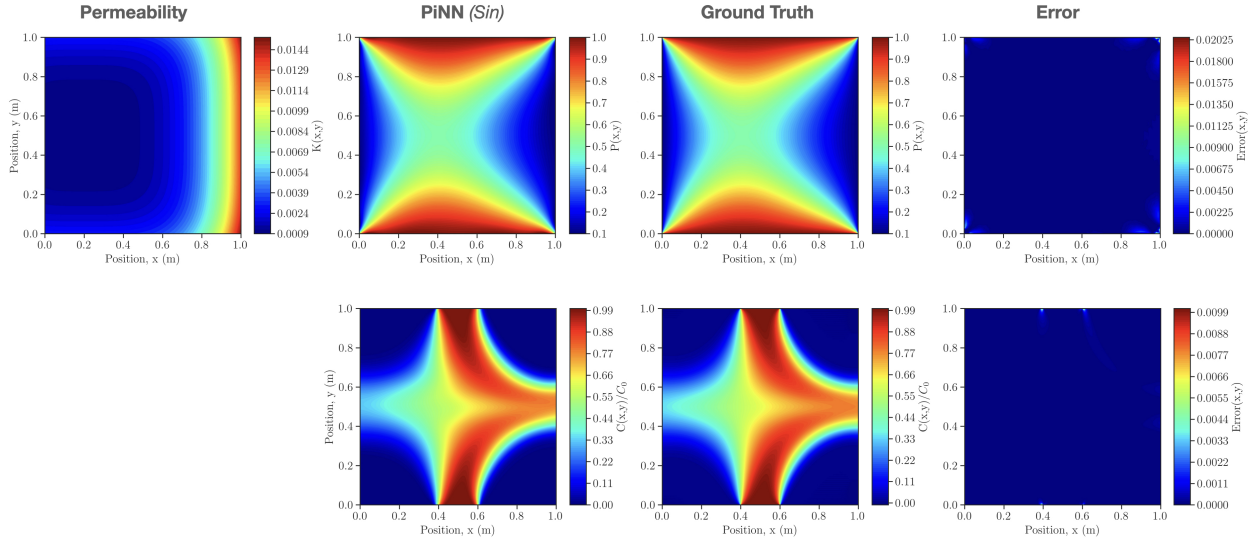


Figure 9: A comparison between the PiNN's predictions and ground truth solutions for solute transport in a heterogeneous porous medium with the given permeability field,  $k(x, y)$ . The comparison is illustrated for the pressure field as well as the concentration field at  $t = 1.00 \text{ s}$  considering  $D_x = D_y = 0.02 \text{ m}^2/\text{s}$ ,  $\alpha = 0$ ,  $\mu\phi = 0.001$ , and  $C_0 = 0.2 \text{ kg}/\text{m}^2$ . The PiNN model here uses the  $\sin$  activation function, and the ground truth solutions are obtained using FEM with  $100 \times 100$  quadrilateral elements. The point-wise error for each field shows that the PiNN, with the  $\sin$  activation function, can accurately predict the complex pressure and concentration fields in heterogeneous porous media. The comparison yields  $MSE = 1.19 \times 10^{-6}$  and  $MSE = 0.45 \times 10^{-6}$  for the pressure field and concentration fields.

A PiNN model with randomly distributed collocation points is deployed to simultaneously predict both the pressure and concentration fields. The best PiNN architecture was determined through a manual hyperparameter tuning approach. This procedure resulted in a network with five hidden layers and  $\{32, 32, 16, 16, 16\}$  neurons per layer using 15,000 spatiotemporal random points within  $0 \leq x, y \leq 1$ ,  $0 \leq t \leq 1$  as collocation points to enforce the PDE loss terms. We also utilized 15,000 spatiotemporal random points to represent the boundary and initial conditions informing the loss terms. To achieve convergence while meeting the boundary condition requirements satisfactorily, we employed  $\omega_{PDE} = 0.7$  as the weights for the PDE loss terms.

Figures 8 and 9 compare the PiNN's predictions with the ground truth (FEM solutions) obtained for the solute transport in the heterogeneous porous medium. The comparison is shown for the steady pressure field



and the concentration field at  $t = 1.00$  s. Figure 8 shows the PiNN’s prediction using the  $\tanh$  activation function validated against the FEM solution with  $100 \times 100$  quadrilateral elements. The point-wise error for each field shows that the PiNN, with the  $\tanh$  activation function, has difficulty to converge to the ground truth solution. The discrepancy is more pronounced in the concentration field, which is originated by the rapid variation of velocity fields due to heterogeneities.

Figure 9 shows the PiNN’s prediction using the  $\sin$  activation function validated against FEM solutions with  $100 \times 100$  quadrilateral elements. The point-wise error is also shown for both fields, which shows a considerable accuracy improvement compared to the PiNN with the  $\tanh$  activation function. The maximum point-wise error for the pressure field is reduced to  $\approx 0.02$  from  $\approx 0.49$ . Also, the maximum point-wise error for the concentration field is reduced to  $\approx 0.01$  from  $\approx 0.13$ . The comparison of the PiNN with the periodic activation function and FEM solutions leads to  $MSE = 1.19 \times 10^{-6}$  and  $MSE = 0.45 \times 10^{-6}$  for the pressure field and concentration field, respectively. As illustrated in Fig. 9, the majority of mismatch in this case still occurs near high gradient areas. These comparative findings show that a PiNN with a periodic activation function can simultaneously solve for the pressure and solute concentration fields in 2D heterogeneous media with a higher degree of accuracy compared to other typical activation function. The results also show that PiNN, in general, decreases the computational complexity tremendously for solute transport phenomena in complex porous media.

Table 1: A comparison of the inference time for PiNN with the  $\sin$  activation function and FEM resolving the solute transport in the 2D homogeneous (Case 3) and heterogeneous (Case 4) porous media. Data is obtained using a 3.00-GHz 48-core Intel Xeon Gold 6248R CPU processor with 128 GB of RAM.

	FEM (s)	PiNN (s)	Speed-up Factor (—)
2D Homogeneous	183.8	0.126	1458.7x
2D Heterogeneous	363.2	0.259	1402.3x

Table 1 compares the inference time for PiNN with the  $\sin$  activation function and FEM resolving the solute transport in the 2D homogeneous (Case 3) and heterogeneous (Case 4) porous media. The speed-up factor achieved is around three orders of magnitude and can considerably escalate when a higher-resolution mesh (i.e., a higher number of elements) is used by the FEM solver; a situation that is often faced in cases with higher levels of heterogeneities. Indeed, in such cases, the number of collection points used by PiNN also increases, which could negatively impact the cost of the training but not the inference time. Therefore, the computational efficiency of PiNN is certainly superior to that of a traditional solver (e.g., FEM) in domains with complex geometry and heterogeneity. It is also notable that PiNN comes with several drawbacks. The two most common drawbacks that were also faced in this study are: (i) PiNN’s learning process and hyperparameter tuning were conducted manually. The training can face gradient vanishing problems, which prohibitively slow down the training phase; and (ii) PiNN did not always converge due to competing non-linear loss terms (e.g., PDE loss terms related to the pressure and concentration fields in addition to the loss terms related to initial/boundary conditions for both of the fields). It requires trials and errors to adjust the loss terms’ weight functions to mitigate the instability. The lack of a theoretical condition or constraint (e.g., Courant number in traditional computational fluid dynamics [62]) to assure convergence is an open research area for investigation. All in all, considering the effectiveness of PiNN in combining scientific computing and DL as well as accelerating computation, the addition of PiNNs to the simulations of porous media flow should be investigated further. For example, a future study could be the assessment of PiNNs to model non-isothermal reactive flows in highly heterogeneous and deformable porous media.

## 5. Conclusions

In this study, we presented the application of physics-informed neural networks (PiNNs) to solve the solute transport problem in homogeneous and heterogeneous porous media governed by the advection-dispersion equation. We constructed PiNN using a periodic activation function to accurately predict the complex pressure and concentration fields as well as reduce the computational cost. Using this modification, the derivative of the network inherits the network’s properties entirely, which enables supervising any derivative of the network with complex physical signals. In order to evaluate the capabilities of the proposed PiNN, we built a number of case studies in both 1D and 2D, each of which possessed homogeneous and/or heterogeneous permeability fields. Using a manual hyperparameter tuning approach, the optimal PiNN architecture for each test case was determined. The point-wise error and mean square error (MSE) metrics were used to evaluate the accuracy of PiNN’s predictions in comparison to the ground truth solutions derived analytically or numerically using FEM. Our findings demonstrated that the proposed PiNN can accurately predict the solute transport phenomenon under different conditions. In addition, the results showed that PiNN’s simultaneous predictions of the pressure and concentration fields in heterogeneous porous media are in good agreement with the ground truth solutions while lowering the computational complexity and expense by three-orders of magnitude.

## 6. Acknowledgements

S.A.F. would like to acknowledge the support by Texas Sate University’s International Research Accelerator Grant (award no. 9000003039).

## 7. Conflict of Interest

The authors declare no conflict of interests.

## References

- [1] Peter G Cook and John-Karl Böhlke. Determining timescales for groundwater flow and solute transport. In *Environmental tracers in subsurface hydrology*, pages 1–30. Springer, 2000. DOI: [https://doi.org/10.1007/978-1-4615-4557-6\\_1](https://doi.org/10.1007/978-1-4615-4557-6_1).
- [2] Irina Gaus, Pascal Audigane, Laurent André, Julie Lions, Nicolas Jacquemet, Pierre Durst, Isabelle Czernichowski-Lauriol, and Mohamed Azaroual. Geochemical and solute transport modelling for co2 storage, what to expect from it? *International journal of greenhouse gas control*, 2(4):605–625, 2008. DOI: <https://doi.org/10.1016/j.ijggc.2008.02.011>.
- [3] Karsten Pruess, Steve Yabusaki, Carl Steefel, and Peter Lichtner. Fluid flow, heat transfer, and solute transport at nuclear waste storage tanks in the hanford vadose zone. *Vadose Zone Journal*, 1(1):68–88, 2002. DOI: <https://doi.org/10.2136/vzj2002.6800>.
- [4] Gerd P Bienert, Jan K Schjoerring, and Thomas P Jahn. Membrane transport of hydrogen peroxide. *Biochimica et Biophysica Acta (BBA)-Biomembranes*, 1758(8):994–1003, 2006. DOI: <https://doi.org/10.1016/j.bbamem.2006.02.015>.
- [5] Erik Kristensen and Kim Hansen. Transport of carbon dioxide and ammonium in bioturbated (nereis diversicolor) coastal, marine sediments. *Biogeochemistry*, 45(2):147–168, 1999. DOI: <https://doi.org/10.1023/A:1006131710076>.
- [6] Xinxin Li, Dianqing Li, Yi Xu, and Xiaobo Feng. A dfn based 3d numerical approach for modeling coupled groundwater flow and solute transport in fractured rock mass. *International Journal of Heat and Mass Transfer*, 149:119179, 2020. DOI: <https://doi.org/10.1016/j.ijheatmasstransfer.2019.119179>.
- [7] Sharul Hasan, Wahid Niasar, Nikolaos K Karadimitriou, Jose RA Godinho, Nghia T Vo, Senyou An, Arash Rabani, and Holger Steeb. Direct characterization of solute transport in unsaturated porous media using fast x-ray synchrotron microtomography. *Proceedings of the National Academy of Sciences*, 117(38):23443–23449, 2020. DOI: <https://doi.org/10.1073/pnas.2011716117>.
- [8] Mojtaba Faraji and Mehdi Mazaheri. Mathematical model of solute transport in rivers with storage zones using nonlinear dispersion flux approach. *Hydrological Sciences Journal*, pages 1–13, 2022. DOI: <https://doi.org/10.1080/02626667.2022.2099280>.
- [9] Xiao-Rong Yang and Yan Wang. Ubiquity of anomalous transport in porous media: Numerical evidence, continuous time random walk modelling, and hydrodynamic interpretation. *Scientific reports*, 9(1):1–11, 2019. DOI: <https://doi.org/10.1038/s41598-019-39363-3>.
- [10] Zhihong Zhao, Lanru Jing, Ivars Neretnieks, and Luis Moreno. Numerical modeling of stress effects on solute transport in fractured rocks. *Computers and Geotechnics*, 38(2):113–126, 2011. DOI: <https://doi.org/10.1016/j.compgeo.2010.10.001>.
- [11] Zhi-hong Zhang, Jia-pei Zhang, Zhan-ying Ju, and Min Zhu. A one-dimensional transport model for multi-component solute in saturated soil. *Water Science and Engineering*, 11(3):236–242, 2018. DOI: <https://doi.org/10.1016/j.wse.2018.09.007>.
- [12] Nikhil Bagalkot and G Suresh Kumar. Effect of nonlinear sorption on multispecies radionuclide transport in a coupled fracture-matrix system with variable fracture aperture: a numerical study. *ISH Journal of Hydraulic Engineering*, 21(3):242–254, 2015. DOI: <https://doi.org/10.1080/09715010.2015.1016125>.
- [13] Peyman Mostaghimi, Min Liu, and Christoph H Arns. Numerical simulation of reactive transport on micro-ct images. *Mathematical Geosciences*, 48(8):963–983, 2016. DOI: <https://doi.org/10.1007/s11004-016-9640-3>.
- [14] P Maheshwari, RR Ratnakar, N Kalia, and V Balakotiah. 3-d simulation and analysis of reactive dissolution and wormhole formation in carbonate rocks. *Chemical Engineering Science*, 90:258–274, 2013. DOI: <https://doi.org/10.1016/j.ces.2012.12.032>.
- [15] Benoit Noetinger, Delphine Roubinet, Anna Russian, Tanguy Le Borgne, Frederick Delay, Marco Dentz, Jean-Raynald De Dreuzy, and Philippe Gouze. Random walk methods for modeling hydrodynamic transport in porous and fractured media from pore to reservoir scale. *Transport in Porous Media*, 115(2):345–385, 2016. DOI: <https://doi.org/10.1007/s11242-016-0693-z>.
- [16] Sunyoung Im, Jonggeon Lee, and Maenghyo Cho. Surrogate modeling of elasto-plastic problems via long short-term memory neural networks and proper orthogonal decomposition. *Computer Methods in Applied Mechanics and Engineering*, 385:114030, 2021. DOI: <https://doi.org/10.1016/j.cma.2021.114030>.
- [17] George Em Karniadakis, Ioannis G Kevrekidis, Lu Lu, Paris Perdikaris, Sifan Wang, and Liu Yang. Physics-informed machine learning. *Nature Reviews Physics*, 3(6):422–440, 2021. DOI: <https://doi.org/10.1038/s42254-021-00314-5>.
- [18] Maziar Raissi, Paris Perdikaris, and George E Karniadakis. Physics-informed neural networks: A deep learning framework for solving forward and inverse problems involving nonlinear partial differential equations. *Journal of Computational physics*, 378:686–707, 2019. DOI: <https://doi.org/10.1016/j.jcp.2018.10.045>.
- [19] Jiequn Han, Arnulf Jentzen, and Weinan E. Solving high-dimensional partial differential equations using deep learning. *Proceedings of the National Academy of Sciences*, 115(34):8505–8510, 2018. DOI: <https://doi.org/10.1073/pnas.1718942115>.
- [20] Jens Berg and Kaj Nyström. A unified deep artificial neural network approach to partial differential equations in complex geometries. *Neurocomputing*, 317:28–41, 2018. DOI: <https://doi.org/10.1016/j.neucom.2018.06.056>.
- [21] Justin Sirignano and Konstantinos Spiliopoulos. Dgm: A deep learning algorithm for solving partial differential equations. *Journal of computational physics*, 375:1339–1364, 2018. DOI: <https://doi.org/10.1016/j.jcp.2018.08.029>.
- [22] Salah A Faroughi, Nikhil Pawar, Celio Fernandes, Subasish Das, Nima K Kalantari, and Seyed Kourosh Mahjour. Physics-guided, physics-informed, and physics-encoded neural networks in scientific computing. *arXiv preprint arXiv:2211.07377*, 2022. DOI: <https://doi.org/10.48550/arXiv.2211.07377>.
- [23] Bart Van Merriënboer, Olivier Breuleux, Arnaud Bergeron, and Pascal Lamblin. Automatic differentiation in ml: Where we are and where we should be going. *Advances in neural information processing systems*, 31, 2018. DOI: <https://doi.org/10.48550/arXiv.1810.11530>.
- [24] Atilim Gunes Baydin, Barak A Pearlmutter, Alexey Andreyevich Radul, and Jeffrey Mark Siskind. Automatic differentiation in machine learning: a survey. *Journal of Machine Learning Research*, 18:1–43, 2018. DOI: <https://doi.org/10.48550/arXiv.1502.05767>.
- [25] Maziar Raissi, Paris Perdikaris, and George Em Karniadakis. Physics informed deep learning (part i): Data-driven solutions of nonlinear partial differential equations. *arXiv preprint arXiv:1711.10561*, 2017. DOI: <https://doi.org/10.48550/arXiv.1711.10561>.

- [26] Maziar Raissi, Alireza Yazdani, and George Em Karniadakis. Hidden fluid mechanics: A navier-stokes informed deep learning framework for assimilating flow visualization data. *arXiv preprint arXiv:1808.04327*, 2018. DOI: <https://doi.org/10.48550/arXiv.1808.04327>.
- [27] Muhammad M Almajid and Moataz O Abu-Al-Saud. Prediction of porous media fluid flow using physics informed neural networks. *Journal of Petroleum Science and Engineering*, 208:109205, 2022. DOI: <https://doi.org/10.1016/j.petrol.2021.109205>.
- [28] John M Hanna, Jose V Aguado, Sebastien Comas-Cardona, Ramzi Askri, and Domenico Borzacchiello. Residual-based adaptivity for two-phase flow simulation in porous media using physics-informed neural networks. *Computer Methods in Applied Mechanics and Engineering*, 396:115100, 2022. DOI: <https://doi.org/10.1016/j.cma.2022.115100>.
- [29] Ehsan Haghighat, Danial Amini, and Ruben Juanes. Physics-informed neural network simulation of multiphase poroelasticity using stress-split sequential training. *Computer Methods in Applied Mechanics and Engineering*, 397:115141, 2022. DOI: <https://doi.org/10.1016/j.cma.2022.115141>.
- [30] QiZhi He, David Barajas-Solano, Guzel Tartakovsky, and Alexandre M Tartakovsky. Physics-informed neural networks for multiphysics data assimilation with application to subsurface transport. *Advances in Water Resources*, 141:103610, 2020. DOI: <https://doi.org/10.1016/j.advwatres.2020.103610>.
- [31] QiZhi He and Alexandre M Tartakovsky. Physics-informed neural network method for forward and backward advection-dispersion equations. *Water Resources Research*, 57(7):e2020WR029479, 2021. DOI: <https://doi.org/10.1029/2020WR029479>.
- [32] Shashank Reddy Vadyala, Sai Nethra Betgeri, and Naga Parameshwari Betgeri. Physics-informed neural network method for solving one-dimensional advection equation using pytorch. *Array*, 13:100110, 2022. DOI: <https://doi.org/10.1016/j.array.2021.100110>.
- [33] Chunwei Zhang, Kazuki Kaito, Yingxue Hu, Anindityo Patmonojaji, Shintaro Matsushita, and Tetsuya Suekane. Influence of stagnant zones on solute transport in heterogeneous porous media at the pore scale. *Physics of Fluids*, 33(3):036605, 2021. DOI: <https://doi.org/10.1063/5.0038133>.
- [34] Shahzad Khan, Sharifah E Alhazmi, Fahad M Alotaibi, Massimiliano Ferrara, and Ali Ahmadian. On the numerical approximation of mobile-immobile advection-dispersion model of fractional order arising from solute transport in porous media. *Fractal and Fractional*, 6(8):445, 2022. DOI: <https://doi.org/10.3390/fractalfract6080445>.
- [35] Xiaomin Zhao and M Nafi Toksoz. Solute transport in heterogeneous porous media. *Massachusetts Institute of Technology. Earth Resources Laboratory*, 1994. DOI: <https://doi.org/10.1017/S0022112084002858>.
- [36] M Th Van Genuchten and WJ Alves. Analytical solutions of the one-dimensional convective-dispersive solute transport equation. *United States. Dept. of Agriculture. Technical bulletin (USA)*, 1982. DOI: <https://doi.org/10.22004/ag.econ.157268>.
- [37] Liwei Sun, Han Qiu, Chuanhao Wu, Jie Niu, and Bill X Hu. A review of applications of fractional advection-dispersion equations for anomalous solute transport in surface and subsurface water. *Wiley Interdisciplinary Reviews: Water*, 7(4):e1448, 2020. DOI: <https://doi.org/10.1002/wat2.1448>.
- [38] Michael Haigh, Luolin Sun, James C McWilliams, and Pavel Berloff. On eddy transport in the ocean. part ii: The advection tensor. *Ocean Modelling*, 165:101845, 2021. DOI: <https://doi.org/10.1016/j.ocemod.2021.101845>.
- [39] Shuai Lou, Shu-sheng Chen, Bo-xi Lin, Jian Yu, and Chao Yan. Effective high-order energy stable flux reconstruction methods for first-order hyperbolic linear and nonlinear systems. *Journal of Computational Physics*, 414:109475, 2020. DOI: <https://doi.org/10.1016/j.jcp.2020.109475>.
- [40] Laurent Talon. On the statistical properties of fluid flows with transitional power-law rheology in heterogeneous porous media. *Journal of Non-Newtonian Fluid Mechanics*, 304:104789, 2022. DOI: <https://doi.org/10.1016/j.jnnfm.2022.104789>.
- [41] Elisa Baioni, Mohaddeseh Mousavi Nezhad, Giovanni Michele Porta, and Alberto Guadagnini. Modeling solute transport and mixing in heterogeneous porous media under turbulent flow conditions. *Physics of Fluids*, 33(10):106604, 2021. DOI: <https://doi.org/10.1063/5.0065734>.
- [42] Brian Berkowitz, Joseph Klafter, Ralf Metzler, and Harvey Scher. Physical pictures of transport in heterogeneous media: Advection-dispersion, random-walk, and fractional derivative formulations. *Water Resources Research*, 38(10):9–1, 2002. DOI: <https://doi.org/10.1029/2001WR001030>.
- [43] Ameya D Jagtap, Ehsan Kharazmi, and George Em Karniadakis. Conservative physics-informed neural networks on discrete domains for conservation laws: Applications to forward and inverse problems. *Computer Methods in Applied Mechanics and Engineering*, 365:113028, 2020. DOI: <https://doi.org/10.1016/j.cma.2020.113028>.
- [44] Ameya D Jagtap and George E Karniadakis. Extended physics-informed neural networks (xpinns): A generalized space-time domain decomposition based deep learning framework for nonlinear partial differential equations. In *AAAI Spring Symposium: MLPS*, 2021. DOI: <https://doi.org/10.4208/cicp.OA-2020-0164>.
- [45] Salvatore Cuomo, Vincenzo Schiano Di Cola, Fabio Giampaolo, Gianluigi Rozza, Maizar Raissi, and Francesco Piccialli. Scientific machine learning through physics-informed neural networks: Where we are and what's next. *arXiv preprint arXiv:2201.05624*, 2022. DOI: <https://doi.org/10.48550/arXiv.2201.05624>.
- [46] Ivan Depina, Saket Jain, Sigurdur Mar Valssson, and Hrvoje Gotovac. Application of physics-informed neural networks to inverse problems in unsaturated groundwater flow. *Georisk: Assessment and Management of Risk for Engineered Systems and Geohazards*, 16(1):21–36, 2022. DOI: <https://doi.org/10.1080/17499518.2021.1971251>.
- [47] Lu Lu, Xuhui Meng, Zhiping Mao, and George Em Karniadakis. Deepxde: A deep learning library for solving differential equations. *SIAM Review*, 63(1):208–228, 2021. DOI: <https://doi.org/10.1137/19M1274067>.
- [48] Vincent Sitzmann, Julien N. P. Martel, Alexander W. Bergman, David B. Lindell, and Gordon Wetzstein. Implicit neural representations with periodic activation functions, 2020. URL <https://arxiv.org/abs/2006.09661>.
- [49] David E Rumelhart, Geoffrey E Hinton, and Ronald J Williams. Learning representations by back-propagating errors. *nature*, 323(6088):533–536, 1986. DOI: <https://doi.org/10.1038/323533a0>.
- [50] Yanan Guo, Xiaoqun Cao, Bainian Liu, and Mei Gao. Solving partial differential equations using deep learning and physical constraints. *Applied Sciences*, 10(17):5917, 2020. DOI: <https://doi.org/10.3390/app10175917>.
- [51] Shengze Cai, Zhiping Mao, Zhicheng Wang, Minglang Yin, and George Em Karniadakis. Physics-informed neural networks (pinns) for fluid mechanics: A review. *Acta Mechanica Sinica*, pages 1–12, 2022. DOI: <https://doi.org/10.1007/s10409-021-01148-1>.
- [52] Dong C Liu and Jorge Nocedal. On the limited memory bfgs method for large scale optimization. *Mathematical programming*, 45(1):503–528, 1989. DOI: <https://doi.org/10.1007/BF01589116>.
- [53] Yoshua Bengio. Gradient-based optimization of hyperparameters. *Neural computation*, 12(8):1889–1900, 2000. DOI: <https://doi.org/10.1162/089976600300015187>.
- [54] Sudhir Kylasa, Fred Roosta, Michael W Mahoney, and Ananth Grama. Gpu accelerated sub-sampled newton's method for convex classification problems. In *Proceedings of the 2019 SIAM International Conference on Data Mining*, pages 702–710. SIAM, 2019. DOI: <https://doi.org/10.1137/1.9781611975673.79>.
- [55] Alan Richardson. Seismic full-waveform inversion using deep learning tools and techniques. *arXiv preprint arXiv:1801.07232*, 2018. DOI: <https://doi.org/10.48550/arXiv.1801.07232>.
- [56] Alberto Olmo, Ahmed Zamzam, Andrew Glaws, and Ryan King. Physics-driven convolutional autoencoder approach for cfd data compressions. *arXiv preprint arXiv:2210.09262*, 2022. DOI: <https://doi.org/10.48550/arXiv.2210.09262>.

- [57] Salvatore Cuomo, Fabio Giampaolo, Stefano Izzo, Carlo Nitsch, Francesco Piccialli, and Cristina Trombetti. A physics-informed learning approach to bernoulli-type free boundary problems. *Computers & Mathematics with Applications*, 128: 34–43, 2022. DOI: <https://doi.org/10.1016/j.camwa.2022.10.003>.
- [58] Karan Shah, Patrick Stiller, Nico Hoffmann, and Attila Cangi. Physics-informed neural networks as solvers for the time-dependent schrödinger equation. *arXiv preprint arXiv:2210.12522*, 2022. DOI: <https://doi.org/10.48550/arXiv.2210.12522>.
- [59] Majid Rasht-Behesht, Christian Huber, Khemraj Shukla, and George Em Karniadakis. Physics-informed neural networks (pinns) for wave propagation and full waveform inversions. *Journal of Geophysical Research: Solid Earth*, 127(5): e2021JB023120, 2022. DOI: <https://doi.org/10.1029/2021JB023120>.
- [60] Jian Guo Zhou. A lattice boltzmann method for solute transport. *International journal for numerical methods in fluids*, 61(8):848–863, 2009. DOI: <https://doi.org/10.1002/fld.1978>.
- [61] Pao-Hsiung Chiu, Jian Cheng Wong, Chinchun Ooi, My Ha Dao, and Yew-Soon Ong. Can-pinn: A fast physics-informed neural network based on coupled-automatic-numerical differentiation method. *Computer Methods in Applied Mechanics and Engineering*, 395:114909, 2022. DOI: <https://doi.org/10.1016/j.cma.2022.114909>.
- [62] Theodoros Atmakidis and Eugeny Y Kenig. A study on the kelvin-helmholtz instability using two different computational fluid dynamics methods. *The Journal of Computational Multiphase Flows*, 2(1):33–45, 2010. DOI: <https://doi.org/10.1260/1757-482X.2.1.33>.